

Anomalous migrating diurnal tides in the MLT region during El Niño in Northern Winter and their possible mechanism

删除[author]: Would El Niño enhance or suppress the

删除[author]: tide

删除[author]: region?

**Yetao Cen^{1,2,3}, Chengyun Yang^{1,2,3*}, Tao Li^{1,2,3*}, Jia Yue^{5,6}, James M. Russell III⁶,
and Xiankang Dou^{1,2,3,4}**

¹CAS Key Laboratory of Geospace Environment, School of Earth and Space Sciences,
University of Science and Technology of China, Hefei, Anhui, China

²Mengcheng National Geophysical Observatory, School of Earth and Space Sciences,
University of Science and Technology of China, Hefei, Anhui, China

³CAS Center for Excellence in Comparative Planetology, University of Science and
Technology of China, Hefei, Anhui, China

⁴School of Electronic Information, Wuhan University, Wuhan, Hubei, China

⁵Catholic University of America, DC, USA

⁶Center for Atmospheric Sciences, Hampton University, Hampton, VA, USA

Correspondence: Chengyun Yang (cy yang@ustc.edu.cn) and Tao Li
(litao@ustc.edu.cn)

Abstract

As observed by SABER (Sounding of the Atmosphere using Broadband Emission Radiometry), the migrating diurnal tide (DW1) in the upper mesosphere and lower thermosphere (MLT) region decreased by ~10% during El Niño in the Northern Hemisphere (NH) winter (December-January-February) from 2002 to 2020. According to the multiple linear regression (MLR) analysis, the linear effects of El Niño on the tropical MLT DW1 are significantly negative in both SABER observations and SD-WACCM (the Specified-Dynamics version of the Whole Atmosphere Community Climate Model) simulations. The DW1 response to El Niño in NH winter is much stronger than annual mean. As suggested by SD-WACCM simulation, Hough mode (1, 1) dominates the DW1 tidal variation in the tropical MLT region. The consistency between the (1, 1) mode in the tropopause region and the MLT region and the downward phase progression from 15 to 100 km indicates the direct upward propagation of DW1 from the excitation source in the troposphere. The suppressed DW1 heating rates in the tropical troposphere (average over ~0-16 km and 35°S-35°N) during the El Niño events contribute to the decreased DW1 tide. To evaluate the effect of the gravity waves (GW) on the tide, the GW forcing is calculated as the GW drag weighted by the phase relation between DW1 GW drag and DW1 tidal wind. The negative GW forcing in the tropical upper mesosphere would significantly suppress the MLT DW1 tide during El Niño winter. This tidal-GW interaction in the MLT region could be a dominant mechanism for DW1 response in the MLT to El Niño. During El Niño winter, the increased ratio of the absolute and planetary vorticity (R) suppresses the waveguide and thus the DW1 amplitude in the subtropical mesosphere. However, the effect of waveguide might play a secondary role due to its relatively weak response.

删除[author]: Previous observations and simulations are controversial as to whether El Niño will increase or decrease

删除[author]: and

删除[author]: region. This study revisited the linear response of the MLT DW1 to

删除[author]: during

删除[author]: based on 19-year satellite observations of Sounding of the Atmosphere using Broadband Emission Radiometry (SABER). The MLT DW1 temperature amplit

删除[author]: , consistent with the results from the simulation of the Specified-Dynamics version of the Whole Atmosphere Community Climate Model (SD-WACCM)

删除[author]: Niño-Southern Oscillation (ENSO)

删除[author]: -WACCM

删除[author]: In the

删除[author]: in

删除[author]: region, as well as

删除[author]: km,

删除[author]: During 7 of 8 El Niño winters from 1979 to 2014, the anomalous amplitudes of the (1, 1) mode are negative in both the tropopause region and MLT region.

删除[author]: The mesospheric latitudinal zonal wind shear anomalies during El Niño winters would lead to a narrower waveguide and prevent

删除[author]: vertical propagation

删除[author]: DW1

删除[author]: . The gravity wave

删除[author]: excited

删除[author]: convection also plays

删除[author]: role

删除[author]: modulating

删除[author]: amplitude.

1 Introduction

Atmospheric solar tides are global-scale variations in meteorological variables (e.g., density, wind, and temperature) with subharmonic periods of a solar day. The migrating diurnal tide is dominant in the tropical mesosphere and lower thermosphere (MLT) region and is characterized by westward travelling zonal wavenumber 1, hereafter denoted as DW1 (Chapman & Lindzen, 1970). DW1 is primarily excited by the absorption of infrared (IR) radiation by water vapour in the troposphere (~0–15 km) (Hagan et al., 2002) and can propagate vertically and reach maximum amplitude in the MLT region (Walterscheid., 1981a; [McLandress et al., 1996](#); Liu & Hagan, 1998; Lu et al., 2009; Liu et al., 2010; Yang et al., 2018). Diurnal migrating tides remain a significant focus of scientific research due to a lack of comprehensive understanding of their seasonal and interannual variabilities. The tidal variation in the MLT region depends on variations in the wave sources, such as the solar heating absorption in the lower atmosphere (Chapman & Lindzen, 1970), and the tidal wave propagation, which is affected by background wind variation, such as the QBO (Forbes and Vincent, 1989; Hagan et al., 1999; [McLandress, 2002a](#); Ramesh et al., 2020; [McLandress, 2002b](#); Mayr and Mengel, 2005). In addition to tidal sources and propagation, tidal variability is also affected by the modulation of interactions with gravity waves (GW) (Liu and Hagan, 1998; Li et al., 2009).

As the dominant interannual variation in the tropical troposphere (Yulaeva and Wallace, 1994), the El Niño-Southern Oscillation (ENSO), which is characterized by anomalous sea surface temperature in the eastern equatorial Pacific Ocean, can cause global-scale perturbations in atmospheric temperature, rainfall, and cloudiness and potentially modulate tidal heating sources in the troposphere (Lieberman et al., 2007). Previous studies have documented that ENSO can influence the troposphere (Yulaeva and Wallace, 1994; Calvo-Fernandez et al., 2004) and the stratosphere and mesosphere (Sassi et al., 2004; Randel et al., 2009; Li et al., 2013 and 2016). As ENSO events tend to reach their maximum in the Northern Hemisphere ([NH](#)) winter, they could potentially significantly impact the MLT tide.

删除[author]: McLandress.,

删除[author]: b

71 According to meridional wind observations from the meteor radar at Jakarta
72 (6.4°S, 106.7°E) and medium-frequency (MF) radar at Tirunelveli (8.7°N, 77.8°E),
73 the tropical diurnal tidal amplitudes in the meridional winds were suppressed during
74 the El Niño winters of 1994/1995 and 1997/1998 (Gurubaran et al., 2005). However,
75 Lieberman et al. (2007) documented a dramatic enhancement of the equatorial diurnal
76 tide during 1997 based on MF radar observations at Kauai, Hawaii (22°N, 154°W),
77 which may be connected to more substantial solar heating absorbed by water vapour
78 during the strong El Niño event of 1997-1998. Notably, the positive diurnal tidal
79 amplitude anomaly became much weaker during the wintertime of 1997/1998 when
80 El Niño reached its maximum. In addition, the diurnal tidal amplitudes were
81 suppressed rather than enhanced during the winters of another 3 El Niño events
82 (1991/1992, 1994/1995, and 2002/2003). Based on the observation from
83 ground-based radars and the Thermosphere Ionosphere Mesosphere Energetics and
84 Dynamics (TIMED)/SABER satellite, Vitharana et al. (2021) documented that the
85 DW1 response to El Niño is negative from 2003-2016 considering all the months.
86 However, the response of DW1 to ENSO is different or even opposite in different
87 seasons as suggested by previous studies (e.g. Liberman et al. 2007; Zhou et al., 2018;
88 Kogure et al., 2021). For instance, Lieberman et al. (2007) reported that a dramatic
89 enhancement of the equatorial diurnal tide during 1997 autumn based on MF radar.
90 From July to October of the strong El Niño of 2015, the equatorial DW1 in the MLT
91 was also dramatically enhanced in SABER (Zhou et al., 2018; Kogure et al., 2021).
92 Thus, calculating the regression by binning the data among different months together
93 may underestimate the actual response of MLT DW1 tide during the particular season.
94 Since ENSO reaches its peak in winter, more pronounced effect in the upper
95 atmosphere are expected during that time. Thus, we focus on the linear response of
96 DW1 to ENSO during the winter in this study.
97 Utilizing the Whole Atmosphere Community Climate Model (WACCM) version
98 4, Pedatella & Liu (2012 and 2013) suggested that El Niño could enhance the MLT
99 DW1 tide during winters due to increased tropospheric radiative forcing. In their

删除[author]: From July to October of
删除[author]: strong El Niño of 2015, the equatorial DW1 in
the MLT was dramatically enhanced, as observed by
删除[author]: satellite (
删除[author]: Similar
删除[author]: Niño
删除[author]: 1997-1998 (Lieberman et al., 2007)
删除[author]: positive anomaly of
删除[author]: diurnal tide amplitude
删除[author]: became much weaker
删除[author]:) or even negative (
删除[author]:

simulation, the QBO signal is not included, and the ENSO events are self-generated. As suggested by the WACCM version 6 simulations with self-generated QBO and ENSO, Ramesh et al. (2020) illustrates the linear response of latitude-pressure variation of DW1-T to the seven predictors including ENSO in four seasons. They suggest that the response of DW1 to ENSO is significantly positive in the equatorial MLT region during the NH winter (Figure 5 in Ramesh et al. 2020). However, Liu et al. (2017) found that DW1 amplitudes are suppressed during the winters of El Niño events based on simulations of the ground-to-topside atmosphere-ionosphere for aeronomy (GAIA) model. Since GAIA is nudged with reanalysis data below 30 km, ENSO events and variations in the lower atmosphere are more realistic. The discrepancies among the model simulations and uncertainties in the observations require further investigation of the DW1 tide-ENSO connection.

删除[author]: there is a positive
删除[author]: MLT
删除[author]: tide
删除[author]: El Niño
删除[author]: Ramesh
删除[author]: .,
删除[author]: .

The response of the MLT DW1 tide to ENSO during the winters is revisited in this study based on the DW1 variation extracted from a long-term temperature dataset observed by the Sounding of the Atmosphere using Broadband Emission Radiometry (SABER) onboard the TIMED (Mertens et al., 2001, 2004, Rezac et al. 2015). The “Specified-Dynamics” version of the WACCM simulation is used to study the possible mechanism. The data and methods are described in section 2. Section 3 presents the observational and model results of the DW1 temperature response to ENSO. In section 4, we examine the possible mechanism that modulates the MLT DW1 tide during ENSO events. Finally, a summary is presented in section 5.

2 Data and Methods

The SABER onboard the TIMED satellite began its observations in January 2002. Kinetic temperature profiles are retrieved from the CO2 limb emission profiles from the tropopause to the lower thermosphere using a full non-LTE inversion (Mertens et al., 2001, 2004, Rezac et al. 2015). The latitude range of SABER observations is from 53° in one hemisphere to 83° in the other, and the latitude coverage flips to the

opposite hemisphere approximately every 60 days. Thus, SABER provides nearly continuous soundings within 53°S and 53°N. This study used version 2.0 temperature data from February 2002 through July 2021 to analyze the DW1 temperature tide in the MLT region. The SABER can complete a nearly 24-hr local time observation within an ~60-day window, which allows us to extract the diurnal tide explicitly.

删除[author]: analyse

The method described by Xu et al. (2007) is utilized to extract the DW1 tide from TIMED/SABER temperature data. Migrating tides can be expressed as

$$\frac{1}{2\pi} \int_0^{2\pi} T(t_{LT}, \lambda) d\lambda = \bar{T}(t_{LT}) + \sum_{n=1}^N T_n^{mtw} \cos(n\omega_0 + \psi_n^{mtw}) + T_{r1} \quad (1)$$

where T is temperature, t_{LT} is local time, λ is longitude, \bar{T} is zonal mean

temperature, $\sum_{n=1}^N T_n^{mtw} \cos(n\omega_0 + \psi_n^{mtw})$ is migrating tides, and T_{r1} is remnant. To

extract tidal components, the daily data are first divided into two groups by local time corresponding to the ascending and descending phases, and then, each group is interpolated into 12 longitude grids, each 30° wide, by fitting with a cubic spline. The next step is to calculate the zonal mean for each day to eliminate the nonmigrating tides as well as the stationary planetary waves. The bimonthly amplitudes and phase information of the migrating tides can be calculated by nonlinear least-squares fitting techniques using data within a 60-day sliding window every month (Xu et al., 2007; Smith et al., 2012; Gan et al., 2014).

The WACCM is a fully coupled chemistry-climate model, which is the high-top atmosphere component of the Community Earth System Model (CESM) (Garcia et al., 2007). In this study, the simulation of the Specified-Dynamics (SD) version of WACCM (SD-WACCM), version 4 is adopted to investigate the ENSO-DW1 tide relationship. The vertical range of SD-WACCM extends from the surface up to ~140 km. The simulated diurnal tide in WACCM4 compares favourably with observations (Lu et al., 2011; Davis et al., 2013). SD-WACCM is nudged to meteorological fields from Modern-Era Retrospective Analysis for Research and Applications (MERRA) reanalysis data in the troposphere and stratosphere (from the surface up to 1 hPa) and then is freely run in the MLT (above 0.3 hPa) (Kunz et al., 2011). Smith et al. (2017)

删除[author]: WACCM

删除[author]: WACCM

discussed the dynamic constraints in SD-~~WACCM~~ and their impact on simulation of the mesosphere in detail. The ENSO-related characteristics in the troposphere and stratosphere in SD-~~WACCM~~ follow those in the reanalysis meteorological fields with relaxation. In this study, the SD-~~WACCM~~ output includes complete diurnal tidal information for temperature, zonal and meridional wind, and heating processes from 1979 to 2014. The simulation also outputs the diurnal components of parameterized GW drag. We note here that the WACCM version 6 simulation was not used in this study due to its opponent response of MLT DW1 to ENSO comparing to SABER observations.

删除[author]: WACCM

删除[author]: WACCM

删除[author]: WACCM

The Niño3.4 index (N3.4), which is the sea surface temperature (SST) anomaly averaged over 120°-170°W and 5°S-5°N (available at https://www.esrl.noaa.gov/psd/gcos_wgsp/Timeseries/Data/Niño34), is used to identify El Niño and La Niña events.

The monthly DW1 can be used as a vector with the ratio as the amplitude and the angle as the phase. To evaluate the variations in both the amplitude and phase of the DW1 tide, the monthly DW1 amplitudes are weighted by projecting the monthly mean vectors onto the climatological mean DW1 vector with the phase difference ~~cos~~ ($\Delta\phi$) (the phase difference is $\Delta\phi = \phi - \phi_{\text{clim}}$) as follows:

删除[author]: cos

$$\text{Amp}_{\text{weighted}} = \text{Amp} * \cos(\omega * (\phi - \phi_{\text{clim}})) \quad (2)$$

where ω ($\omega = 2\pi/24$) is the frequency of the DW1 tide. ϕ and ϕ_{clim} are the DW1 phase of each month and the climatological mean, respectively. In the remainder of this study, the weighted DW1 amplitude (and its anomaly) refer to the DW1 amplitude (anomaly) for conciseness. The mean tidal amplitude and phase during ~~NH~~ winter are derived from the averaged tidal vectors for December, January, and February (DJF) of each year.

删除[author]: northern

To derive the winter interannual variability that may be related to ENSO, we first calculate the DW1 anomalies by removing the climatological mean seasonal cycle.

Then, the winter (DJF) mean of the DW1 anomalies is calculated. Natural forcing, such as the solar cycle (represented by F107), QBO, ENSO, and long-term trends, jointly affect the DW1 tidal amplitude (e.g., Dhadly et al., 2018; Gurubaran et al., 2005; Gurubaran & Rajaram, 1999; Hagan et al., 1999; Lieberman et al., 2007; Liu et al., 2017; Pedatella & Liu, 2012; Sridharan, 2019, 2020; Sridharan et al., 2010; Vincent et al., 1998; Xu et al., 2009). To isolate the linear forcing of ENSO from the interference of other factors, a multivariate linear regression (MLR) analysis is applied on the anomalous time series at each latitude and altitude, the same as that used in Li et al. (2013).

$$T(t) = C_1 * \text{Niño3.4} + C_2 * \text{QBO10} + C_3 * \text{QBO30} + C_4 * \text{F107} + C_5 * \text{TREND} + \varepsilon(t) \quad (3)$$

where T is the DW1-T anomaly, t is time, C1–C5 are regression coefficients, and ε is the residual; QBO10 and QBO30 are two orthogonal QBO time series derived from the zonal wind (m s^{-1}) averaged over 5°N to 5°S at 10 and 30 hPa (Wallace et al., 1993), respectively. The Niño3.4 index (Niño3.4) is the 3-month running mean of SST averaged over 5°N to 5°S , 120°W – 170°W ; F107 is the solar radio flux at 10.7 cm, which is a proxy for solar activity; and TREND is the long-term linear trend. The linear contribution of each factor during winters is determined by applying MLR to DJF anomalies each year. The analysis is carried out for the period of 2002–2020 at each latitude and pressure grid point. The F test (Kissell et al., 2017) was used to evaluate the statistical significance of the regression coefficients.

The Hough function in classic tidal theory ([Chapman & Lindzen, 1970](#)), which represents the solution of the Laplace tide equation in the isothermal atmosphere, can set a consistent latitude variation in the amplitude and phase of the tidal perturbation field. The Hough functions of daily variation frequency form a complete orthogonal set and extend from 90°S to 90°N . This method of estimating amplitude and phase is based on fitting the Hough mode to the zonal structure representation and the simple harmonic function (sine and cosine) to the local time-varying representation. The Hough mode is represented as $\Theta_{s,n}(\theta)$, or (s, n), where s indicates the zonal wavenumber and index n is positive for gravitational modes (propagating modes) and

删除[author]: Lindzen and Chapman

删除[author]: 1969

negative for rotational modes (trapped modes). The normalized functions satisfy the following relation

$$\int_{-90^{\circ}}^{90^{\circ}} \Theta_{1,n}(\theta) \bullet \Theta_{1,m}(\theta) \cos(\theta) d\theta = \begin{cases} 1, m = n \\ 0, m \neq n \end{cases}, n, m = \pm 1, \pm 2, \dots \quad (4)$$

3 Results

As presented in Figure 1a, the NH winter (December-January-February, DJF) mean amplitude of DW1 in temperature extracted from TIMED/SABER observation is largest (~12 K) in the equatorial mesopause region during 2002-2013. Although the amplitude is smaller, the distribution of the DW1 T amplitude in SD-WACCM simulation (Figure 1b) is similar to that derived from SABER observation, with the maximum at 90-100 km above the equator. There are some differences between SABER and SD-WACCM: SABER has a weaker peak above the equator at 70-80 km, but this peak cannot be seen in SD-WACCM.

Figures [2a](#) and [2b](#) show the monthly mean DW1 temperature amplitude anomalies (removing the climatological mean seasonal cycle) averaged over 10°S-10°N at 100 km derived from SABER observations and SD-~~WACCM~~ simulations between 2002 and 2020, respectively. Among the analyzed period, there were 4 El Niño events in 2002, 2006, 2009, and 2015, which are indicated with red arrows and defined by the Niño3.4 index in Figure [2c](#); the 3 La Niña events in 2007, 2010, and 2020 are indicated with blue arrows. The anomalous DW1 amplitudes are negative during 4 El Niño winters and positive during all 3 La Niña events. The DW1 anomalies reach a positive maximum in July to October during the 2015/2016 strong El Niño event, which agrees with Zhou et al. ([2018](#)); however, they become negative in winter. In the period when SD-~~WACCM~~ and SABER overlap (2002-2014), the simulated DW1 amplitude anomalies in SD-~~WACCM~~ are negative during all 3 El Niño winters (2002, 2006, and 2009) and positive during 2 La Niña events. The

删除[author]: 1
删除[author]: 1b
删除[author]: WACCM
删除[author]: analysed
删除[author]: 1c
删除[author]: 2020
删除[author]: WACCM
删除[author]: WACCM

239 negative response of the MLT DW1 tide to El Niño in the SD-WACCM simulation
240 agrees well with that in the SABER observation.

241 In the 35-yr SD-WACCM simulations (1979-2014), the anomalous DW1
242 amplitudes averaged over 10°S-10°N at 100 km are negative during 7 of 8 El Niño
243 winters (1982, 1986, 1991, 1997, 2002, 2006, and 2009), as shown in Table 1. The
244 MLR coefficients of DW1 to normalized Niño3.4 are significantly negative in both
245 the SABER observation and SD-WACCM simulation, as shown in Figure 3. The
246 amplitude of DW1 in the equatorial region is significantly reduced, however the phase
247 anomaly is not drifted much (less than 1 hour) during El Niño winter. (figure S1, S2).

248 The MLT DW1 response to El Niño in winter is five times stronger than the
249 average response in SABER observations derived by Vitharana et al (2021). This is
250 due to the fact that the DW1 enhancement in El Niño autumn (e.g. Liberman et al.
251 2007; Zhou et al., 2018; Kogure et al., 2021) may weaken the negative response to
252 ENSO. In the simulations of Ramesh et al. (2020), different seasons also exhibit
253 different responses of DW1 to ENSO. The MLR coefficients of tropical DW1 to
254 Niño3.4 in the SABER observation (with a minimum of ~ -1 K/index) are twice as
255 strong as those (with a minimum of ~ -0.5 K/index) in the SD-WACCM simulation
256 since the magnitude of the DW1 tide is underestimated in the WACCM4 simulation
257 (Liu et al., 2010; Lu et al., 2012). The negative response of the MLT DW1-T
258 amplitude to El Niño is consistent with early MF radar/meteor radar observations and
259 GAIA model simulations with a nudging process (Gurubaran, 2005 and Liu et al.,
260 2017) but opposite to free-run WACCM simulations (Pedatella & Liu 2012 and
261 2013).

262 The MLR coefficients of the DW1 response to normalized QBO10 and QBO30
263 in the equatorial mesopause region are significantly positive, with a minimum of ~ 1
264 K/(m*s⁻¹) near 100 km (Figure S3), consistent with previous studies (Ramesh et al.
265 2020). The linear effects of the QBO on the MLT DW1 tides are comparable to those
266 of ENSO (the variances in the DW1 tide explained by ENSO, QBO10, and QBO30

删除[author]: WACCM

删除[author]: WACCM

删除[author]: 2

删除[author]: S1

删除[author]: 2021

267 are 23%, 20%, and 17%, respectively). The interaction between the QBO and ENSO
268 may potentially modulate the ENSO-DW1 tide relationship ([Gray, 1984](#)). In this study,
269 we focused on the linear effect of ENSO on the MLT DW1 tidal variability and the
270 associated mechanism. In SD-WACCM, the linear regression coefficients of DW1 are
271 a negative response to Niño3.4 and a positive response to QBO10 and QBO30, which
272 is consistent with the SABER observation, although the absolute value of the
273 coefficients decreases more than that of SABER. The variance percentages of F107
274 are negligible compared with these three variables. In the remainder of this study,
275 only the linear effect of ENSO on the MLT DW1 tide is discussed.

删除[author]: Grey

删除[author]: 1988

4 Possible Mechanisms

4.1 Tidal forcing and propagation

A specific tidal component, such as DW1, can be decomposed into a series of gravity wave-like modes and Rossby wave-like modes based on the Hough functions (Figure S4) (Auclair-Desrotour et al., 2017; Chapman & Lindzen, 1970; Forbes, 1995). In a qualitative sense, the tidal response can be considered a combination of GWs restored by stable stratification and inertial Rossby waves due to Coriolis acceleration. The Hough modes of the DW1 tide in the SD-WACCM simulation are analysed to examine the mechanism of tropical DW1 tidal variation. As shown in Figure 4a, the anomalies of the DW1 temperature amplitude averaged over 10°S-10°N at 100 km are consistent with its Hough (1,1) component (the correlation coefficient between MLT DW1-T anomalies and its Hough (1,1) component is 0.99) during the NH winter from 1979 to 2013. The DW1-T amplitude anomalies and their Hough (1,1) component during El Niño years decrease by 15% compared to the climatological mean amplitude. During winters (DJF) from 1979 to 2013, the average phase of DW1-T over 10°S-10°N shows general downward phase progression with the height from the MLT region to the tropopause region (approximately 15 km). This kind of downward phase advance with height implies an upward group velocity for the vertically propagating gravity model. By tracking the downward phase progressive line, the altitude of the excitation source is estimated to be below 15 km. The DW1-T phase during El Niño winters corresponds with the climatological mean phase structure, implying that ENSO-induced tidal perturbation in the troposphere could directly propagate vertically into the MLT region. The anomalous Hough (1,1) mode of the DW1 temperature amplitude at MLT (100 km) is significantly correlated (the correlation coefficient is 0.81) with that at the tropopause region (15 km), indicating the effective propagation of the perturbation in the tropospheric Hough (1,1) into the MLT region. During 7 of 8 El Niño events (1982, 1986, 1991, 1997, 2002, 2006, and 2009), the Hough (1,1) mode at 100 km is ~10% smaller than that in the tropopause,

删除[author]: S2

删除[author]: WACCM

删除[author]: 3a

删除[author]: Northern Hemisphere (

删除[author]:)

which agrees well with the suppressed Hough (1,1) in the MLT.

As noted earlier, the DW1 tide is primarily excited by the absorption of solar radiation by tropospheric water vapour (Lieberman et al., 2003; Zhang et al., 2010). According to the tidal theory (Volland and Hans, 1988), the heating rate of radiation absorbed by water vapour in the entire troposphere is responsible for the excitation of diurnal migrating tides. Next, we examine the perturbation of the DW1 solar heating source in the SD-~~WACCM~~ simulation, which potentially contributes to the negative Hough (1,1) tidal anomalies in the tropopause region during El Niño winters. As presented in Figure 5, the anomalous amplitudes of the DW1 heating rate (HR) regressed on the normalized Niño3.4 index are significantly positive (with a maximum of ~ 0.4 mW/m³ per index) in the upper tropical troposphere (5°S-5°N, 3-12 km) but are significantly negative below 3 km (with a minimum of ~ -4 mW/m³ per index). The ENSO-induced changes in the tropospheric DW1 heating forcing may be due to the redistribution of tropospheric convection during El Niño and La Niña winters. During El Niño winters, increased moisture in the upper troposphere due to enhanced tropical precipitation in the central Pacific Ocean (e.g., Hoerling et al., 1997) leads to stronger solar heating absorption by water vapour in the middle and upper equatorial troposphere (5–12 km, 10°S–10°N). On the other hand, heating in the lower troposphere significantly decreased due to less solar radiation below the convective cloud. The DW1 HR regressed on Niño3.4 in the NH (5°N-35°N) is characterized by a significantly negative coefficient of 3-8 km (with a maximum of ~ -0.3 mW/m³ per index) associated with significantly positive coefficients below 2 km (with a maximum of ~ 3 mW/m³ per index). In the Southern Hemisphere (SH), the distribution of DW1 HR coefficients consists of negative and positive values at different altitudes and latitudes.

Pedatella et al. (2013) adopted the HR in the upper tropical troposphere (5-10 km within $\pm 20^\circ$) to estimate the ENSO-induced variation in the DW1 tidal source. Other studies suggested the HR in both the upper and lower troposphere (e.g., altitude range

删除[author]: WACCM

删除[author]: 4

between 900-200 hPa, 1-12 km in Lieberman et al., 2003, and 1000-100 hPa, 0-16 km in Zhang et al., 2010). As suggested by Table 2, the mass-weighted HR averaged over the entire tropical troposphere (0-16 km, 35°N-35°S), which negatively responds to ENSO, is significantly correlated (the correlation coefficient is 0.45) with the DW1 tide in the tropical tropopause region. Although the linear regression coefficient in HR is positive at 5-10km over the equator (5°N-5°S), the coefficients at 5-30°N(S) are negative (Figure 5), which is opposite of the equator (5°N-5°S). The HR averaged over 5-10 km, 20°N-20°S (the same as in Pedatella et al., 2013) regressed on Niño3.4 is also negative, although it is not significantly correlated with the DW1 tidal variation in the tropopause. The decreased DW1 heating source in the troposphere during El Niño is a primary cause of the suppressed DW1 tide in the tropopause region winters, which propagates vertically and affects the DW1 tidal variation in the MLT region.

4.2 Effect of background wind

The zonal wind in the middle atmosphere can modulate tide propagation from the troposphere to the MLT (Forbes and Vincent, 1989). As McLandress (2002b) described, the perturbation latitudinal shear in the zonal mean zonal wind (zonal mean vorticity) can affect DW1 propagation into the MLT region by causing departures from classical tidal dynamics. The zonal mean vorticity $\bar{\zeta}$ and Coriolis parameter f are given by the following equation:

$$\bar{\zeta} = \frac{-1}{a \cos \theta} * \frac{\partial(\bar{u} \cos \theta)}{\partial \theta} \quad (5)$$

$$f = 2\Omega \sin \theta \quad (6)$$

$$R = (\bar{\zeta} + f)/f \quad (7)$$

where a , \bar{u} and θ correspond to the Earth radius, zonal mean zonal wind and latitude, respectively, and Ω is the Earth's rotation rate.

The ratio of the absolute and planetary vorticity R is equivalent to changing the planet rotation rate. In classical theory, the vertically propagating DW1 is restricted near the equator due to the planet's rapid rotation. Therefore, a faster rotation rate (positive R anomalies) will suppress the latitudinal band (i.e., waveguide) where DW1 can propagate vertically. On the other hand, the slower rotation rate (negative R anomalies) favors the vertical propagation and is thus able to enhance the amplitude of DW1 at the low latitudes (McLandress, 2002b). When the ratio of the absolute and planetary vorticity R -value at a certain height becomes larger, the upward propagation of tide is suppressed, which lead to weaker tides above there.

The MLR coefficient of R on Niño3.4 is illustrated in Figure 6. Below 60 km, the ratio R exhibits negative and positive responses to ENSO depending on different altitudes in the northern and southern subtropics. The R response to ENSO is positive at 60-100 km in the northern subtropics, and 65-100 km in the southern subtropics is positive. The green thick solid line represents the mean value of the equatorial R (15-30°N and 15-30°S), and it can be seen that the mean R value response to ENSO is significantly positive at 60-90 km. The increased ratio R in the mesosphere results in suppressed latitudinal band, which prevents the upward propagation of the DW1 tide during El Niño winters. The correlation coefficient between the R value and DW1 during the winter of 1979-2014 is -0.33 (significant at 95% level) in the SH, and is -0.37 (significant at 95% level) in the NH the correlation coefficient, both of which are significantly correlated. The significantly negative correlation between R and DW1 tide implies that the R plays a role in modulation the upward propagating of DW1 when no ENSO event occurs. The variation of R and DW1 should not be attributed to the impacts of ENSO separately.

删除[author]: In
删除[author]: . The ratio of the absolute and planetary vorticity R can be regarded as an enhancement of the Coriolis parameter f in the linearized tidal equations in
删除[author]: simple way. A larger
删除[author]: indicates that
删除[author]: becomes narrower
删除[author]:),
删除[author]: DW1
删除[author]: (Wu et al., 2017). Conversely
删除[author]: a smaller ratio of R would benefit
删除[author]: DW1
删除[author]: 5
删除[author]: 50
删除[author]: 55
删除[author]: 85

4.3 Effect of gravity wave forcing

In addition to tidal sources and tidal propagation, MLT tidal variability is also affected by interactions with GWs (Liu and Hagan, 1998; Li et al., 2009). GWs are the main driving force of MLT dynamic activity, which has an essential influence on tidal amplitude and phase (Walterscheid, 1981b; Lu et al., 2012; Liu et al., 2013). The effect of the GW forcing on tides is not fully understood due to the limited observation and lack of high-resolution model simulations that can fully resolve both tides and GWs. In WACCM, the GWs are parameterized, and their tropical sources are interactive and mainly triggered by convection in the tropics (Beres et al., 2005). The GW in the tropics is primarily induced by the convection, while the GW in the middle to high latitudes is mainly generated by the frontal systems (Figure S5, S6). Due to this source of interaction, the GW drag will likely be modulated by ENSO as the location and size of the ENSO-related convection change. The GW drag far away from the tropospheric source has a strong response to the wind. As mentioned above, we can determine the variation in the resistance of the convection-generated GW in the WACCM. We mainly focus on the latitudinal component of parameterized resistance because it is usually much larger than the meridional component (Yang et al. 2018).

In the NH winter, the amplitude of the DW1 zonal GW drag caused by convection has obvious hemispheric asymmetry: the magnitude is much smaller in the NH than in the SH (Figure 7a). The zonal wind DW1 tidal can be written as
 $U' = A^* \cos(\omega^*(t - \varphi) - s\lambda)$, where A and φ are the amplitude and phase of DW1
tide, ω ($\omega = 2\pi/24$) is DW1 frequency, λ is longitude and s ($s = 2\pi/360$) is
zonal wave number of DW1. The time tendency of zonal wind can be written as:

$$\frac{\partial U'}{\partial t} = \omega^* A^* \cos(\omega^*(t - \varphi) + \frac{\pi}{2} - s\lambda) = \omega^* A^* \cos(\omega^*(t - (\varphi - 6)) - s\lambda); \quad (8)$$

The phase of the DW1 tide time trend leads the tide itself by 6 hours. To evaluate the effect of GW forcing on the DW1 tide during DJF, the GW forcing can be calculated as:

$$GW_{\text{forcing}} = GW_{\text{drag}} * \cos(\omega * (\varphi_{GW} - (\varphi_U - 6))); \quad (9)$$

Where GW_{drag} is GW drag, and φ_{GW} and φ_U are the phase of DW1-GW and DW1-U.

The convection-generated DW1 GW forcing on the DW1 tide is positive in the southern subtropical upper mesosphere and negative below this tide (60–80 km) during the NH winter (Figure 7b). In the NH, the DW1 GW forcing of the DW1 tide is positive in the subtropical mesosphere (15–35°N, 80–100 km) and negative in the tropical mesosphere (0–10°N, 80–100 km), indicating that convection-generated GW forcing will dampen the tides in the tropical MLT and enhance the tides in the NH and SH subtropical regions (Figure 7b). As shown in Figure 8a, the correlation between DW1 U and GW drag from 1979 to 2014 winter (DJF) is only significant in the mesopause region of southern subtropical and equator. The correlation between DW1 U and GW forcing from 1979 to 2014 winter (DJF) is larger than 0.7 in the tropical and subtropical MLT (Figure 8b) and the grey areas indicates statistical significance below 95% level using Student's t test, which means GW forcing is clearly modulate the tide, especially in the Southern subtropics. The linear regression coefficient of Niño3.4 in the GW forcing is significantly negative in the tropical MLT region (Figure 9, 80–100 km), suggesting that the decreased GW forcing would lead to a weaker DW1 U amplitude during El Niño winters.

Although parameterized GWs are excited by convection, it is difficult to find a direct cause and effect relationship between ENSO-related tropospheric changes and the GW-induced tidal forcing in the mesosphere. The GW forcing in the MLT not only depends on the generation of waves in the troposphere but also on zonal wind filtering when they propagate upward from the troposphere to the upper mesosphere.

删除[cyt]: To evaluate the effect of convection-generated GW forcing on the DW1 tide during DJF, the GW forcing needs to be projected into the time tendency of DW1-U. The phase of the DW1 tide time trend leads the tide by 6 hours; thus, the GW forcing can be calculated as follows:

$$GW_{\text{forcing}} = GW_{\text{drag}} * \cos(\omega * (\varphi_{GW} - (\varphi_U - 6)));$$

where GW_{drag} is the GW drag, φ_{GW} and φ_U are the phases of DW1-GW and DW1-U, and ω ($\omega = 2\pi/24$) is the DW1 frequency.

删除[author]: S3

删除[author]: S3

删除[author]: S4)

删除[author]: 6

430 However, our study suggests that the ENSO modulation of tidal amplitude can come
431 not only from the disturbance in tropospheric tidal sources and tidal propagation
432 modulated by zonal wind but also from the disturbance of the GW-tidal interaction in
433 the upper mesosphere.

434

435 **5 Discussion and Summary**

436 The response of the MLT DW1 tide to ENSO is investigated during the northern
437 winter when ENSO reach its peak, by using satellite observations of temperature
438 profiles and the SD-WACCM simulation. The DW1 amplitude of temperature
439 observed by the SABER tends to decrease during the NH winter of 4 El Niño events
440 from 2002 to 2020 when El Niño reaches its peak and increase during 3 La Niña
441 events. In SD-WACCM simulations, the DW1 amplitude is suppressed during 7 of 8
442 El Niño winter (DJF) events from 1979 to 2014. ▽

443 Possible mechanisms have been proposed to explain the DW1 response to ENSO:
444 (1) the source of tidal excitation in the lower atmosphere and its upward propagation,
445 (2) the impact from background wind variation on the tidal propagation, and (3)
446 interaction between gravity waves and tides. As the Hough (1,1) mode dominates the
447 diurnal migrating tidal temperature in the MLT region, its negative response to ENSO
448 corresponds well with the counterpart at the tropopause. By tracking the downward
449 phase progressive line, the altitude of the excitation source is estimated to be below
450 15 km. The decreased heating rate in the tropical troposphere (35°S-35°N, 0-16 km)
451 during El Niño peaks contribute to the suppressed DW1 tidal amplitude in the tropical
452 tropopause.

453 As the background variation could modulate the upward propagation of the tide
454 (Forbes and Vincent, 1989; McLandress, 2002a, 2002b), the ratio of the absolute and
455 planetary vorticity R response to ENSO is investigated. The R response to ENSO is
456 significantly positive anomalous at 60-90 km, leading to the narrower waveguide and

删除[author]: ENSO effects on the

删除[author]: in the MLT region are

删除[author]: both

删除[author]: The

删除[author]: component

删除[author]: DW1-T variation

删除[author]: propagating vertically from 15 km

删除[author]: 100

删除[author]: HR of

删除[author]: whole

删除[author]: ,

删除[author]: decreased

删除[author]: Niño peaks, corresponding

删除[author]: troposphere

删除[author]: ENSO modulates DW1 propagation by
affecting

删除[author]: wind field in

删除[author]: middle atmosphere. The

删除[author]: and

删除[author]: linearly affected by Niño3.4

删除[author]: positive

457 resulting in weaker DW1 amplitude above. However, the regression coefficient of R
458 on the ENSO index is relatively small compared to the mean value of R, which imply
459 that the impact of R on tidal propagation may play a secondary role in the
460 ENSO-DW1 connection.

删除[author]: subtropical mesosphere

删除[author]: suppresses

删除[author]: waveguide

461 In addition to tidal sources and tidal propagation, MLT tidal variability is also
462 dramatically affected by interactions with GWs (Liu and Hagan, 1998; Li et al., 2009).
463 GW forcing considering both the DW1 tidal GWs drag and the phase difference with
464 the DW1 tide, is calculated to evaluate the effect of the GW variation on the tide
465 during ENSO winters. The GW forcing response to Niño3.4 is significantly negative
466 in the tropical upper mesosphere, which suggests the GW response to ENSO tends to
467 dampen the MLT DW1 tide during El Niño winter. This tidal-GW interaction could
468 significantly modulate the tidal amplitude as revealed by early lidar observations (Li
469 et al., 2009; Baumgarten et al., 2018). This could be most important mechanism of
470 DW1 response in the MLT region to ENSO. However, quantitative evaluation of this
471 interaction is out of scope of this paper and needs far more sophistic model with
472 extreme high resolution to self-generate convective GWs.

删除[author]: thus

删除[author]: amplitude during El Niño winter. In addition

删除[author]: suppressing

473 The weak negative DW1 response to ENSO over the equator may be related to
474 the dissipation or damping of the tide near 95 km. The shorter vertical wavelength
475 would increase the Rayleigh friction coefficient proportional (Forbes et al., 1989),
476 which result in enhancement of the tide dissipation. As presented in Table S1, the
477 vertical wavelength of DW1 near 95 km is increased (but decreased at around 90 and
478 100 km), which would suppress the Rayleigh friction coefficient and lead to less tidal
479 dissipation. Therefore, the less tidal dissipation in this area could result in a relatively
480 weak negative or even positive response to ENSO near 95 km. The interaction of
481 gravity waves and tides may also play a role in modulating the tidal amplitude at
482 different altitudes. However, the SD-WACCM simulation failed to perform a similar
483 tidal response near 95 km as SABER observations. Further investigation with more

484 detailed GW from observation or the improved GW parameterization scheme and
485 higher vertical resolution in model simulation are need.

486

487 **Data availability**

488 SABER dataset are available at <http://saber.gats-inc.com/data.php>, ECMWF
489 dataset used here are obtained at <http://apps.ecmwf.int/datasets/data>.

490

491 **Author contributions**

492 YC and CY designed the study, performed data analysis, prepared the figures and
493 wrote the manuscript. TL initiated the study and contributed to supervision and
494 interpretation. JY and JR contributed to editing the manuscript. XD contributed to
495 interpretation. All authors contributed to discussion and interpretation.

496

497 **Competing interests**

498 The authors declare that they have no conflict of interest.

499

500 **Acknowledgments**

501 This work was funded by the National Natural Science Foundation of China
502 grants (42130203, 41974175, 41874180), and the B-type Strategic Priority Program
503 of the Chinese Academy of Sciences, Grant No. XDB41000000. JY and JMR's work
504 is supported by the National Science Foundation grant AGS-1901126.

Reference

- Auclair-Desrotour, P. , Laskar, J. , & Mathis, S. (2017). Atmospheric tides and their consequences on the rotational dynamics of terrestrial planets. *EAS Publications Series*, 82 (2019) 81-90. <https://doi.org/10.1051/eas/1982008>
- Baumgarten, Kathrin, Gerding, Michael, Gerd, & Luebken, et al. (2018). Temporal variability of tidal and gravity waves during a record long 10-day continuous lidar sounding. *Atmospheric chemistry and physics*, 18, 371–384, 2018 <https://doi.org/10.5194/acp-18-371-2018>
- Beres, J. H., Garcia, R. R., Boville, B. A., & Sassi, F. (2005). Implementation of a gravity wave source spectrum parameterization dependent on the properties of convection in the Whole Atmosphere Community Climate Model (WACCM). *Journal of Geophysical Research*, 110, D10108. <https://doi.org/10.1029/2004JD005504>
- Calvo-Fernández, Natalia, Herrera, Ricardo García, Puyol, D. G. , Martín, Emiliano Hernández, García, Rolando R., & Presa, L. G. , et al. (2004). Analysis of the enso signal in tropospheric and stratospheric temperatures observed by msu, 1979-2000. *Journal of Climate*, 17(20), 3934-3946. [http://doi.org/10.1175/1520-0442\(2004\)017<3934:aotesi>2.0.co;2](http://doi.org/10.1175/1520-0442(2004)017<3934:aotesi>2.0.co;2)
- Chapman, S., & Lindzen, R. S., *Atmospheric Tides*, 201 pp., D. Reidel, Norwell, Mass., 1970.
- Davis, R. N., Du, J., Smith, A. K., Ward, W. E., & Mitchell, N. J. (2013). The diurnal and semidiurnal tides over Ascension Island (8°S, 14°W) and their interaction with the stratospheric QBO: Studies with meteor radar, eCMAM and WACCM. *Atmospheric Chemistry and Physics*, 13(18), 9543–9564. <https://doi.org/10.5194/acp-13-9543-2013>
- Dhadly, M. S., Emmert, J. T., Drob, D. P., McCormack, J. P., & Niciejewski, R. (2018). Short-term and interannual variations of migrating diurnal and semidiurnal tides in the mesosphere and lower thermosphere. *Journal of Geophysical Research: Space Physics*, 123, 7106–7123.

535 <https://doi.org/10.1029/2018JA025748>

536 [Forbes, J. M. . \(1995\). Tidal and planetary waves. *Geophysical Monograph Series*, 87.](#)

537 <https://doi.org/10.1029/GM087p0067>

538 [Forbes, J. M. , & Vincent, R. A. . \(1989\). Effects of mean winds and dissipation on the](#)

539 [diurnal propagating tide: an analytic approach. *Planetary & Space Science*, 37\(2\),](#)

540 [197-209. \[https://doi.org/10.1016/0032-0633\\(89\\)90007-X\]\(https://doi.org/10.1016/0032-0633\(89\)90007-X\)](#)

541 Gan, Q., Du, J., Ward, W. E., Beagley, S. R., Fomichev, V. I., & Zhang, S. (2014).

542 Climatology of the diurnal tides from eCMAM30 (1979 to 2010) and its

543 comparisons with SABER. *Earth Planets Space* 66:103,

544 <https://doi.org/10.1186/1880-5981-66-103>

545 Garcia, R. R., Marsh, D. R., Kinnison, D. E., Boville, B. A., & Sassi, F. (2007).

546 Simulation of secular trends in the middle atmosphere, 1950–2003.

547 *Journal of Geophysical Research*, 112, D09301.

548 <https://doi.org/10.1029/2006JD007485>

549 Gray, W. M., Atlantic seasonal hurricane frequency: Part I: El Niño and 30 mb

550 quasi-biennial oscillation influences. *Mon. Wea. Rev.*, 112, 1649–1668, 1984

551 [https://doi.org/10.1175/1520-0493\(1984\)112<1649:ASHFPI>2.0.CO;2](https://doi.org/10.1175/1520-0493(1984)112<1649:ASHFPI>2.0.CO;2)

552 Gurubaran, S., & Rajaram, R. (1999). Long-term variability in the mesospheric tidal

553 winds observed by MF radar over Tirunelveli (8.7°N, 77.8°E). *Geophysical*

554 *Research Letters*, 26(8), 1113–1116. <https://doi.org/10.1029/1999GL900171>

555 Gurubaran, S., Rajaram, R., Nakamura, T., & Tsuda, T. (2005). Interannual variability

556 of diurnal tide in the tropical mesopause region: a signature of the El

557 Niño-Southern Oscillation (ENSO). *Geophysical Research Letters* 32(13):

558 <https://doi.org/10.1029/2005gl022928>

559 Hagan, M.E., Burrage, M.D., Forbes, J.M. et al. (1999). QBO effects on the diurnal

560 tide in the upper atmosphere. *Earth Planet Space*, 51, 571–578,

561 [doi:/10.1186/BF03353216](https://doi.org/10.1186/BF03353216)

562 [Hagan, M. E., and J. M. Forbes. \(2002\). Migrating and nonmigrating diurnal tides in](#)

563 [the middle and upper atmosphere excited by tropospheric latent heat release, *J.*](#)

564 [Geophys. Res.](#), 107(D24), 4754, <https://doi.org/10.1029/2001JD001236>.

删除[author]:

Garcia-Herrera, R., N. Calvo, R. R. Garcia, and M. A. Giorgetta (2006), Propagation of ENSO temperature signals into the middle atmosphere: A comparison of two general circulation models and ERA-40 reanalysis data, *J. Geophys. Res.*, 111, D06101, <https://doi.org/10.1029/2005JD006061>.

删除[author]: Nino

删除[author]: Hagan, M. E., Burrage, M. D., Forbes, J. M., Hackney, J., Randel, W. J., & Zhang, X. (1999). GSWM-98: Results for migrating solar tides. *Journal of Geophysical Research*, 104(A4), 6813–6827. <https://doi.org/10.1029/1998JA900125>

<p>565 Hoerling, M. P., A. Kumar, and M. Zhong. (1997), El Niño, La Niña, and the</p> <p>566 nonlinearity of their teleconnections, <i>Journal of Climate</i>, 10, 1769–1786.</p> <p>567 <a href="https://doi.org/10.1175/1520-0442(1997)010<1769:ENOLNA>2.0.CO;2">https://doi.org/10.1175/1520-0442(1997)010<1769:ENOLNA>2.0.CO;2</p> <p>568 Kissell, R. & Poserina, J. (2017). Optimal Sports Math, Statistics, and Fantasy.</p> <p>569 https://doi.org/10.1016/B978-0-12-805163-4.00002-5</p> <p>570 Kogure, M., & Liu, H. (2021). DW1 tidal enhancements in the equatorial MLT during</p> <p>571 2015 El Niño: The relative role of tidal heating and propagation. <i>Journal of</i></p> <p>572 <i>Geophysical Research: Space Physics</i>, 126, e2021JA029342.</p> <p>573 https://doi.org/10.1029/2021JA029342</p> <p>574 Kunz, A., Pan, L., Konopka, P., Kinnison, D., & Tilmes, S. (2011). Chemical and</p> <p>575 dynamical discontinuity at the extratropical tropopause based on START08 and</p> <p>576 WACCM analyses. <i>Journal of Geophysical Research</i>, 116, D24302.</p> <p>577 https://doi.org/10.1029/2011JD016686</p> <p>578 Lieberman, R. S., Ortland, D. A., & Yarosh, E. S. (2003). Climatology and</p> <p>579 interannual variability of diurnal water vapor heating. <i>Journal of Geophysical</i></p> <p>580 <i>Research: Atmospheres</i> 108(D3): https://doi.org/10.1029/2002jd002308</p> <p>581 Lieberman, R. S., Riggin, D. M., Ortland, D. A., Nesbitt, S. W., & Vincent, R. A.</p> <p>582 (2007). Variability of mesospheric diurnal tides and tropospheric diurnal heating</p> <p>583 during 1997–1998. <i>Journal of Geophysical Research: Atmospheres</i> 112(D20):</p> <p>584 https://doi.org/10.1029/2007jd008578</p> <p>585 Li, T., She, C. -Y., Liu, H., Yue, J., Nakamura, T., Krueger, D. A., et al. (2009).</p> <p>586 Observation of local tidal variability and instability, along with dissipation of</p> <p>587 diurnal tidal harmonics in the mesopause region over Fort Collins, Colorado</p> <p>588 (41°N, 105°W). <i>Journal of Geophysical Research: Atmospheres</i> (1984–2012),</p> <p>589 114(D6). https://doi.org/10.1029/2008jd011089</p> <p>590 Li, T., Calvo, N., Yue, J., Dou, X., Russell III, J. M., Mlynczak, M. G., She, C.-Y., &</p> <p>591 Xue, X. (2013). Influence of El Niño-Southern Oscillation in the mesosphere.</p> <p>592 <i>Geophysical Research Letters</i>, 40, 3292–3296, https://doi.org/10.1002/grl.50598.</p> <p>593 Li, T., Calvo, N., Yue, J., Russell, J. M. I., Smith, A. K., Mlynczak, M. G., Chandran,</p> <p>594 A., Dou, X., & Liu, A. Z. (2016). Southern Hemisphere summer mesopause</p>	<p>删除[author]: Hays, P. B., & Wu, D.L. (1994). Observations of the diurnal tide from space. <i>Journal of the Atmospheric Sciences</i>, 51(20):3077–3093, ...</p> <p>删除[author]: Nina</p> <p>删除[author]: Huang, F. T.</p> <p>删除[author]: Mayr, H. G., Reber, C</p> <p>删除[author]: A.</p> <p>删除[author]: Russell, J., Mlynczak, M., & Mengel, J. (2006)</p> <p>删除[author]: Zonal-mean temperature variations inferred from SABER measurements on TIMED compared with UARS observations. <i>Journal of Geophysical Research: Atmosphere</i> ...</p> <p>删除[author]: W., Holland</p> <p>删除[author]: M.</p> <p>删除[author]: Gent</p> <p>删除[author]: P</p> <p>删除[author]: R., Ghan, S., Kay, J. E., Kushner, P. J., et al. (2013</p> <p>删除[author]: The Community Earth System Model</p> <p>删除[author]: A framework for collaborative research</p> <p>删除[author]: Bulletin</p> <p>删除[author]: the American Meteorological Society</p> <p>删除[author]: 94(9)</p> <p>删除[author]: 1339-1360</p> <p>删除[author]: Masaru Kogure, Huixin Liu (2021). DW1 Tidal Enhancements in the equatorial MLT during 2015 El Niño: The relative r ...</p> <p>删除[author]: Lindzen, R. S., and S. Chapman (1969), Atmospheric tides, <i>Space Science Review</i>, 10(1), 3–188</p> <p>删除[author]: (</p>
--	--

595 responses to El Niño-Southern Oscillation. *Journal of*
 596 *Climate*, 29(17), 6319– 6328. <https://DOI.org/10.1175/JCLI-D-15-0816.1>

597 Liu, A. Z., Lu, X., & Franke, S. J. (2013). Diurnal variation of gravity wave
 598 momentum flux and its forcing on the diurnal tide. *Journal of Geophysical*
 599 *Research – Atmospheres*, 118, 1668–1678.
 600 <https://doi.org/10.1029/2012JD018653>

601 Liu, H., Sun, Y.-Y., Miyoshi, Y., & Jin, H. (2017). ENSO effects on MLT diurnal
 602 tides: A 21 year reanalysis data-driven GAIA model simulation. *Journal of*
 603 *Geophysical Research: Space Physics*, 122, 5539–5549,
 604 <https://doi.org/10.1002/2017JA024011>.

605 Liu, H.-L., Wang, W., Richmond, A. D., & Roble, R. G. (2010). Ionospheric
 606 variability due to planetary waves and tides for solar minimum conditions.
 607 *Journal of Geophysical Research: Space Physics*, 115, A00G01,
 608 <https://doi.org/10.1029/2009JA015188>.

609 Liu, H.-L., & Hagan, M. E. (1998). Local heating/cooling of the mesosphere due to
 610 gravity wave and tidal coupling. *Geophysical Research Letters*, 25, 2941–2944
 611 <https://doi.org/10.1029/98GL02153>

612 Lu, X., Liu, A. Z., Swenson, G. R., Li, T., Leblanc, T., & McDermid, I. S. (2009).
 613 Gravity wave propagation and dissipation from the stratosphere to the lower
 614 thermosphere. *Journal of Geophysical Research: Atmospheres*, 114, D11101,
 615 <https://doi.org/10.1029/2008JD010112>.

616 Lu, X., Liu, H.-L., Liu, A. Z., Yue, J., McInerney, J. M., & Li, Z. (2012). Momentum
 617 budget of the migrating diurnal tide in the Whole Atmosphere Community
 618 Climate Model at vernal equinox. *Journal of Geophysical Research*, 117,
 619 D07112. <https://doi.org/10.1029/2011JD017089>

620 Lu, X., Liu, A. Z., Oberheide, J., Wu, Q., Li, T., Li, Z., et al. (2011). Seasonal
 621 variability of the diurnal tide in the mesosphere and lower thermosphere over
 622 Maui, Hawaii (20.7°N, 156.3°W). *Journal of Geophysical Research*, 116,

623 D17103. <https://doi.org/10.1029/2011JD015599>
 624 Mayr H.G., Mengel J.G. (2005). Interannual variations of the diurnal tide in the
 625 mesosphere generated by the quasi-biennial oscillation, *J Geophys Res*
 626 *110:D10111*. doi:10.1029/2004JD005055
 627 McLandress, C., Shepherd, G. G., & Solheim, B. H. (1996). Satellite observations of
 628 thermospheric tides: Results from the wind imaging interferometer on UARS.
 629 *Journal of Geophysical Research: Atmospheres* 101(D2):4093–4114,
 630 <https://doi.org/10.1029/95jd03359>
 631 McLandress, C. (2002a). Interannual variations of the diurnal tide in the mesosphere
 632 induced by a zonal- mean wind oscillation in the tropics, *Geophys. Res. Lett.*,
 633 29(9), doi:10.1029/2001GL014551.
 634 McLandress, C. (2002b), The seasonal variation of the propagating diurnal tide in the
 635 mesosphere and lower thermosphere. Part II: The role of tidal heating and zonal
 636 mean winds, J. Atmos. Sci., 59(5), 907–922,
 637 [https://doi.org/10.1175/1520-0469\(2002\)059<0907:Tsvotp>2.0.Co;2](https://doi.org/10.1175/1520-0469(2002)059<0907:Tsvotp>2.0.Co;2).
 638 Mertens, C. J., Mlynczak, M. G., Lopez-Puertas, M., Wintersteiner, P. P., Picard, R.
 639 H., Winick, J. R., & Gordley, L. L. (2001). Retrieval of mesospheric and lower
 640 thermospheric kinetic temperature from measurements of CO₂ 15 μm Earth
 641 limb emission under non-LTE conditions, *Geophysical Research Letters*, 28(7),
 642 1391-1394. <https://doi.org/10.1029/2000GL012189>
 643 Mertens, C. J., Schmidlin, F. J., Goldberg, R. A., Remsberg, E. E., Pesnell, W. D.,
 644 Russell, J. M., Mlynczak, M. G., Lopez-Puertas, M., Wintersteiner, P. P., Picard,
 645 R. H., Winick, J. R., & Gordley, L. L. (2004). SABER observations of
 646 mesospheric temperatures and comparisons with falling sphere measurements
 647 taken during the 2002 summer MaCWAVE campaign. *Geophysical Research*
 648 *Letters* 31(3). <https://doi.org/10.1029/2003gl018605>
 649 Pedatella, N. M., & Liu, H. L. (2012). Tidal variability in the mesosphere and lower
 650 thermosphere due to the El Niño-Southern Oscillation. *Geophysical Research*
 651 *Letters* 39. <https://doi.org/10.1029/2012gl053383>

删除[author]: Oberheide, J., Forbes, J. M., Zhang, X., &
 Bruinsma, S. L. (2011). Climatology of upward propagating
 diurnal and semidiurnal tides in the thermosphere. *Journal of*
Geophysical Research: Space Physics, 116, A11306.
<https://doi.org/10.1029/2011JA016784>

652 Pedatella, N. M., & Liu, H. L. (2013). Influence of the El Niño Southern Oscillation
653 on the middle and upper atmosphere. *Journal of Geophysical Research:*
654 *Atmospheres* 118(5):2744–2755, <https://doi.org/10.1002/Jgra.50286>
655 Ramesh, K., Smith, A. K., Garcia, R. R., Marsh, D. R., Sridharan, S., & Kishore
656 Kumar, K. (2020). Long-term variability and tendencies in migrating diurnal tide
657 from WACCM6 simulations during 1850–2014. *Journal of Geophysical*
658 *Research: Atmospheres*, 125, e2020JD033644.
659 <https://doi.org/10.1029/2020JD033644>
660 Randel, W. J. , Shine, K. P. , Austin, J. , Barnett, J. , Claud, C. , & Gillett, N. P. , et al.
661 (2009). An update of observed stratospheric temperature trends. *Journal of*
662 *Geophysical Research: Atmospheres*. 114, D02107,
663 <https://doi.org/10.1029/2008JD010421>
664 Rezac, L., Y. Jian, J. Yue, J. M. Russell III, A. Kutevov, R. Garcia, K. Walker, and
665 P. Bernath (2015), Validation of the global distribution of CO2 volume mixing
666 ratio in the mesosphere and lower thermosphere from SABER, *J. Geophys. Res.*
667 *Atmos.*, 120, 12,067– 12,081.
668 <https://doi.org/10.1002/2015JD023955>.
669 Sassi, F., Kinnison, D., Boville, B., Garcia, R., Roble, R. (2004). Effect of el
670 niño-southern oscillation on the dynamical, thermal, and chemical structure of
671 the middle atmosphere. *Journal of Geophysical Research*, 109(D17), D17108.
672 <http://doi.org/10.1029/2003jd004434>
673 Smith, A. K. (2012). Global Dynamics of the MLT. *Surveys in Geophysics*, 33(6):
674 1177–1230, <https://doi.org/10.1007/s10712-012-9196-9>
675 Smith, A. K., Pedatella, N. M., Marsh, D. R., & Matsuo, T. (2017). On the Dynamical
676 Control of the Mesosphere–Lower Thermosphere by the Lower and Middle
677 Atmosphere, *Journal of the Atmospheric Sciences*, 74(3), 933-947.
678 <https://doi.org/10.1175/JAS-D-16-0226.1>
679 Sridharan, S., Tsuda, T., & Gurubaran, S. (2010). Long-term tendencies in the
680 mesosphere/lower thermosphere mean winds and tides as observed by
681 medium-frequency radar at Tirunelveli (8.7° N, 77.8° E). *Journal of Geophysical*

删除[author]: Sun
删除[author]: Y
删除[author]: Y
删除[author]: Liu
删除[author]: H
删除[author]: Miyoshi
删除[author]: Y
删除[author]: Liu
删除[author]: L
删除[author]: Chang
删除[author]: L
删除[author]: C
删除[author]: (2018)

682 Research: Atmospheres, 115(D8).
683 <http://doi.org/10.1029/2008JD011609>, 2010
684 Sridharan, S. (2019). Seasonal variations of low-latitude migrating and nonmigrating
685 diurnal and semidiurnal tides in TIMED-SABER temperature and their
686 relationship with source variations. *Journal of Geophysical Research: Space*
687 *Physics*, 124, 3558–3572.
688 <https://doi.org/10.1029/2018JA026190>
689 Sridharan, S. (2020). Equatorial upper mesospheric mean winds and tidal response to
690 strong El Niño and La Niña. *Journal of Atmospheric and Solar-Terrestrial*
691 *Physics*, 202, 105270.
692 <https://doi.org/10.1016/j.jastp.2020.105270>
693 Vincent, R. A., Kovalam, S., Fritts, D. C., & Isler, J. R. (1998). Long-term MF radar
694 observations of solar tides in the low-latitude mesosphere: Interannual variability
695 and comparisons with GSWM. *Journal of Geophysical Research*, 103(D8),
696 8667–8683. <https://doi.org/10.1029/98JD00482>
697 Vitharana, A., Du, J., Zhu, X., Oberheide, J., & Ward, W. E. (2021). Numerical
698 prediction of the migrating diurnal tide total variability in the mesosphere and
699 lower thermosphere. *Journal of Geophysical Research: Space Physics*, 126,
700 e2021JA029588. <https://doi.org/10.1029/2021JA029588>
701 Volland & Hans. *Atmospheric Tidal and Planetary Waves*[M]. Springer Netherlands,
702 1988
703 Wallace, J. M., Panetta, R. L., & J. Estberg (1993). Representation of the equatorial
704 quasi-biennial oscillation in EOF phase space. *Journal of the Atmospheric*
705 *Sciences*, 50, 1751 – 1762,
706 [https://doi.org/10.1175/1520-0469\(1993\)050<1751:ROTESQ>2.0.CO;2](https://doi.org/10.1175/1520-0469(1993)050<1751:ROTESQ>2.0.CO;2).
707 Walterscheid, R. L. (1981a). Inertia-gravity wave induced accelerations of mean flow
708 having an imposed periodic component: Implications for tidal observations in the
709 meteor region. *Journal of Geophysical Research: Atmospheres*, 86, 9698 – 9706.
710 <https://doi.org/10.1029/JC086iC10p09698>

删除[author]: El Niño-Southern Oscillation effect on
quasi-biennial oscillations

删除[author]: temperature

删除[author]: the mesosphere

删除[author]: lower thermosphere

删除[author]: Earth Planets Space

删除[author]: [1186/s40623-018-0832-6](https://doi.org/10.1186/s40623-018-0832-6)

删除[author]: Wallace J. M. , & Hobbs P. V., *Atmospheric
science*, 2006

Walterscheid, R. L. (1981b). Dynamical cooling induced by dissipating internal gravity waves. *Geophysical Research Letters*, 8(12), 1235 – 1238.
<https://doi.org/10.1029/GL008i012-p01235>

Xu, J. Y., Liu, H. L., Yuan, W., Smith, A. K., Roble, R. G., Mertens, C. J., Russell, J. M., & Mlynczak, M. G. (2007a). Mesopause structure from thermosphere, ionosphere, mesosphere, energetics, and dynamics (TIMED)/sounding of the atmosphere using broadband emission radiometry (SABER) observations. *Journal of Geophysical Research: Atmospheres* 112 (D9).
<https://doi.org/10.1029/2006jd007711>

Xu, J. Y., Smith, A. K., Yuan, W., Liu, H. L., Wu, Q., Mlynczak, M. G., Russell, J. M. (2007b). Global structure and long-term variations of zonal mean temperature observed by TIMED/SABER. *Journal of Geophysical Research: Atmospheres*, 112, D24106: <https://doi.org/10.1029/2007jd008546>

Xu, J., A. K. Smith, H.-L. Liu, W. Yuan, Q. Wu, G. Jiang, M. G. Mlynczak, J. M. Russell III, and S. J. Franke (2009), Seasonal and quasi-biennial variations in the migrating diurnal tide observed by Thermosphere, Ionosphere, Mesosphere, Energetics and Dynamics (TIMED), *J. Geophys. Res.*, 114, D13107, doi:10.1029/2008JD011298.

Yang, C., Smith, A. K., Li, T., & Dou, X. (2018). The effect of the Madden-Julian oscillation on the mesospheric migrating diurnal tide: A study using SD-WACCM. *Geophysical Research Letters*, 45, 5105–5114.
<https://doi.org/10.1029/2018GL077956>

Yulaeva, E., & Wallace, J. M. (1994). The signature of ENSO in global temperature and precipitation fields derived from the microwave sounding unit. *Journal of climate*, 7(11), 1719-1736.
[https://doi.org/10.1175/1520-0442\(1994\)007<1719:TSOEIG>2.0.CO;2](https://doi.org/10.1175/1520-0442(1994)007<1719:TSOEIG>2.0.CO;2)

Zhang, X., Forbes, J. M., & Hagan, M. E. (2010). Longitudinal variation of tides in the MLT region: 1. Tides driven by tropospheric net radiative heating. *Journal of Geophysical Research: Space Physics* , 115, A06316,
<https://doi.org/10.1029/2009JA014897>.

删除[author]: Warner, K., Oberheide, J. (2014) Nonmigrating tidal heating and MLT tidal wind variability due to the El Niño-Southern Oscillation. *Journal of Geophysical Research: Atmospheres* 119:1249–1265.
<https://doi.org/10.1002/2013JD020407>

删除[author]: , Li
 删除[author]: T., Dou, X., & Xue, X. (2015). Signal of central Pacific El Niño in the Southern Hemispheric stratosphere during Austral spring. *Journal of Geophysical Research: Atmospheres*, 120,11,438–11,450. <https://doi.org/10.1002/2015JD023486>.
 Yang, C.,

741 Zhou, X., Wan, W., Yu, Y., Ning, B., Hu, L., and Yue, X. (2018). New approach to
742 estimate tidal climatology from ground-and space-based observations. *Journal of*
743 *Geophysical Research: Space Physics*, 123, 5087– 5101.
744 doi:10.1029/2017JA024967

745

746

Table 1. The list of ENSO years with corresponding Niño3.4 indices and anomaly DW1 temperature amplitudes of the SD-WACCM simulations averaged over 10°S-10°N at 100 km.

El Niño events	Niño3.4 index	SD-WACCM anomalous DW1 T AMP (K)
1982-1983	2.14	-0.22
1986-1987	1.11	-2.90
1991-1992	1.69	-1.56
1994-1995	1.22	1.56
1997-1998	2.33	-1.87
2002-2003	1.37	-0.55
2006-2007	1.09	-1.30
2009-2010	1.43	-1.82
AVG	1.54	-0.96

Table 2. The correlation coefficient between the DW1 T amplitude at 15 km and the mass-weighted HR in different areas during the winters of 1979-2014. The bold numbers indicate that the correlation coefficients are significant at the 95% level. The MLR coefficient on the normalized Niño3.4 index (10^{-3} mw m⁻³ index⁻¹) is also exhibited.

Altitude and latitude ranges	0-16 km, 35°N-35°S)	0-12 km, 35°N-35°S)	5-10 km, 35°N-35°S)	5-10 km,20° N-20°S)
Correlation coefficient	0.45	0.36	0.32	0.32
MLR coefficient on Niño3.4	-3	-10	-26	-9

756 **Figure captions**

757 **Figure 1.** (a) The average DW1 temperature amplitude of SABER observation during 2002-2013
758 winter (DJF, Dec-Jan-Feb). (b) the same as (a), but for SD-WACCM.

删除[author]: .

759 **Figure 2.** (a) The residual DW1 temperature amplitude of SABER observations averaged over
760 10°S-10°N at 100 km during 2002-2021. (b) Same as in (a) but for SD-WACCM. (c) Niño3.4
761 index. Dashed lines represent ENSO events. The red and blue arrows denote the El Niño and La
762 Niña events, respectively.

763 **Figure 3.** The linear regression coefficient of normalized Niño3.4 in SABER (a) and SD-WACCM
764 (b) winter DW1-T. The contour interval is 0.2 K for SABER and 0.1 K for SD-WACCM. Red
765 represents a positive response, and blue represents a negative response; the grey regions denote
766 confidence levels below 95% for the F test.

删除[author]: 2

删除[author]: .

767 **Figure 4.** (a) The red line indicates the anomalous DW1 temperature amplitude of SD-WACCM
768 simulations averaged over 10°S-10°N at 100 km during the 1979-2013 winter (DJF). The blue line
769 indicates the Hough (1,1) mode of the DW1 temperature amplitude residual at 100 km during the
770 1979-2013 winter (DJF). (b) The thin black line indicates the Hough (1,1) DW1-T phase of
771 SD-WACCM simulations at 0-100 km during the 1979-2013 winter (DJF). The thick black
772 horizontal line indicates the standard deviation of the DW1-T phase. The red line is the same but
773 for El Niño winter. (c) The blue line is the same as in (a), and the black line is the same but for 15
774 km.

删除[author]: 3

775 **Figure 5.** The linear regression coefficient of normalized Niño3.4 in SD-WACCM heating
776 amplitude (mW/m³ per index) during 1979-2013 winters (DJF). Red represents a positive response,
777 and blue represents a negative response; the grey regions denote confidence levels below 95%
778 according to the F test.

删除[author]: 4

779 **Figure 6.** The linear regression coefficient of normalized Niño3.4 in δR (the anomaly of the ratio
780 of the absolute and planetary vorticity). The thin, dashed red, blue and green lines denote the
781 averages of the Northern Hemisphere (from 15°N to 30°N), Southern Hemisphere (from 15°S to
782 30°S) and the whole (15-30°N and 15-30°S) , respectively. The thick, solid lines denote
783 confidence levels below 95% for the F test.

删除[author]: 5

删除[author]: , δR

删除[author]: thick

删除[author]: solid red

删除[author]: blue

删除[author]: and

784 **Figure 7.** (a) Gravity Wave (GW) drag due to convection on the amplitude of DW1 tidal U during

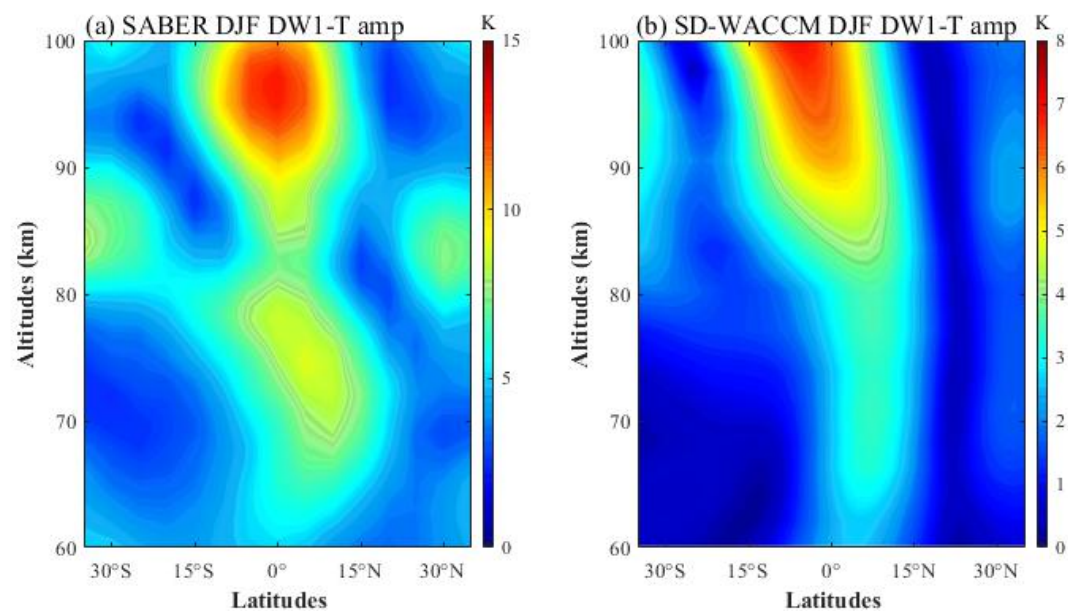
删除[author]: 6

the winter (DJF). (b) The same as (a), but for GW forcing.

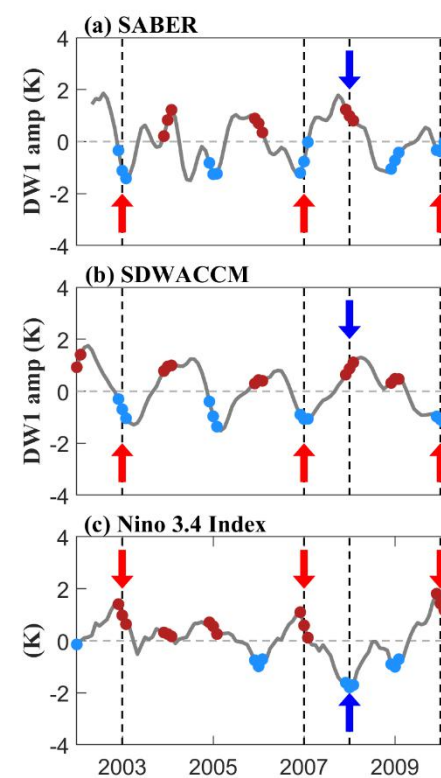
Figure 8. Correlation (a) between DW1 U and GW drag, (b) between DW1 U and GW forcing from 1979 to 2014 winter (DJF).

Figure 9. The linear regression coefficient of normalized Niño3.4 in the GW forcing on the amplitude of DW1-U during 1979-2013 winters (DJF). Red represents a positive response, and blue represents a negative response; the grey regions denote confidence levels below 95%.

793 **Figures**



795 **Figure 1.** (a) The average DW1 temperature amplitude of SABER observation during 2002-2013
796 winter (DJF, Dec-Jan-Feb). (b) the same as (a), but for SD-WACCM.



删除[author]:

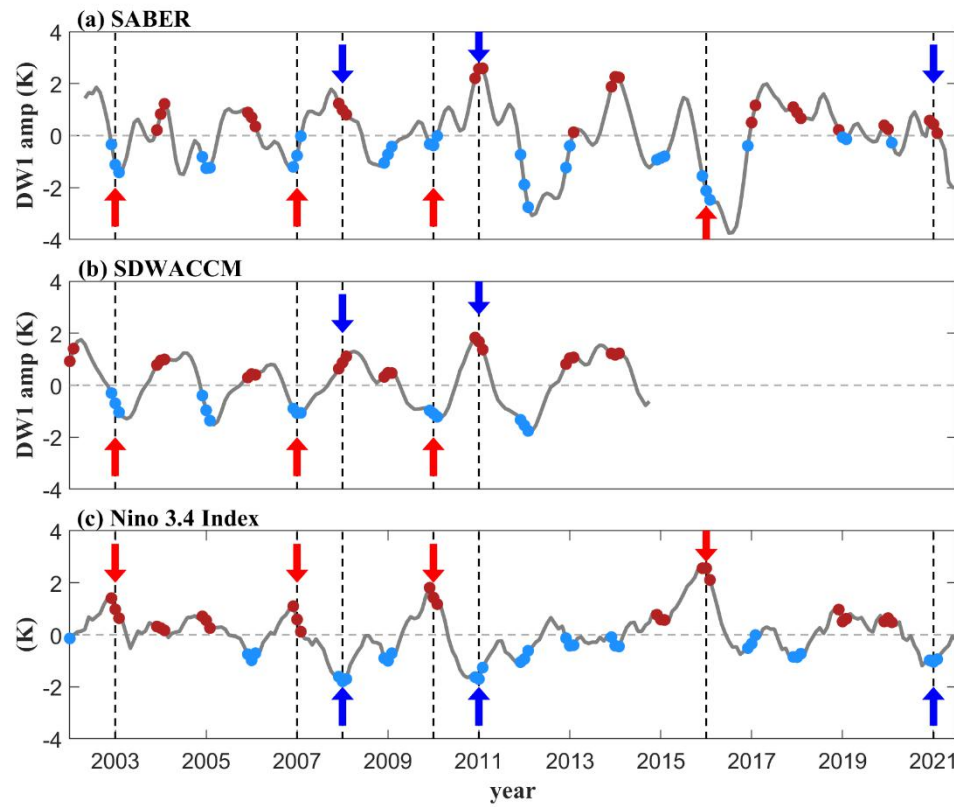
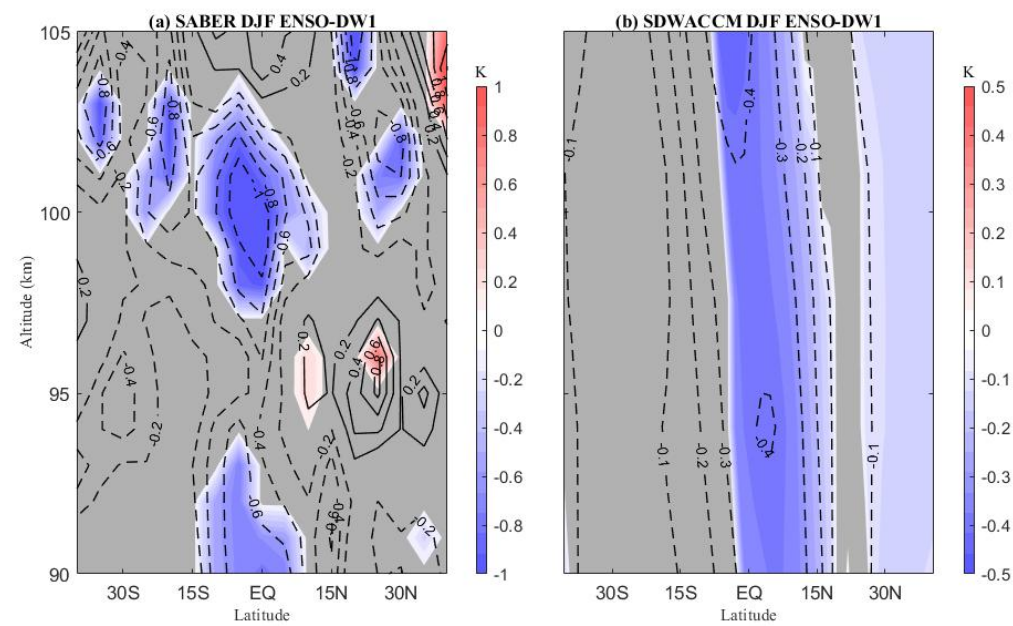


Figure 2. (a) The residual DW1 temperature amplitude of SABER observations averaged over 10°S-10°N at 100 km during 2002-2021. (b) Same as in (a) but for SD-WACCM. (c) Niño3.4 index. Dashed lines represent ENSO events. The red and blue arrows denote the El Niño and La Niña events, respectively.

804



805

806 **Figure 3.** The linear regression coefficient of normalized Niño3.4 in SABER (a) and SD-WACCM

807 (b) winter DW1-T. The contour interval is 0.2 K for SABER and 0.1 K for SD-WACCM. Red

808 represents a positive response, and blue represents a negative response; the grey regions denote

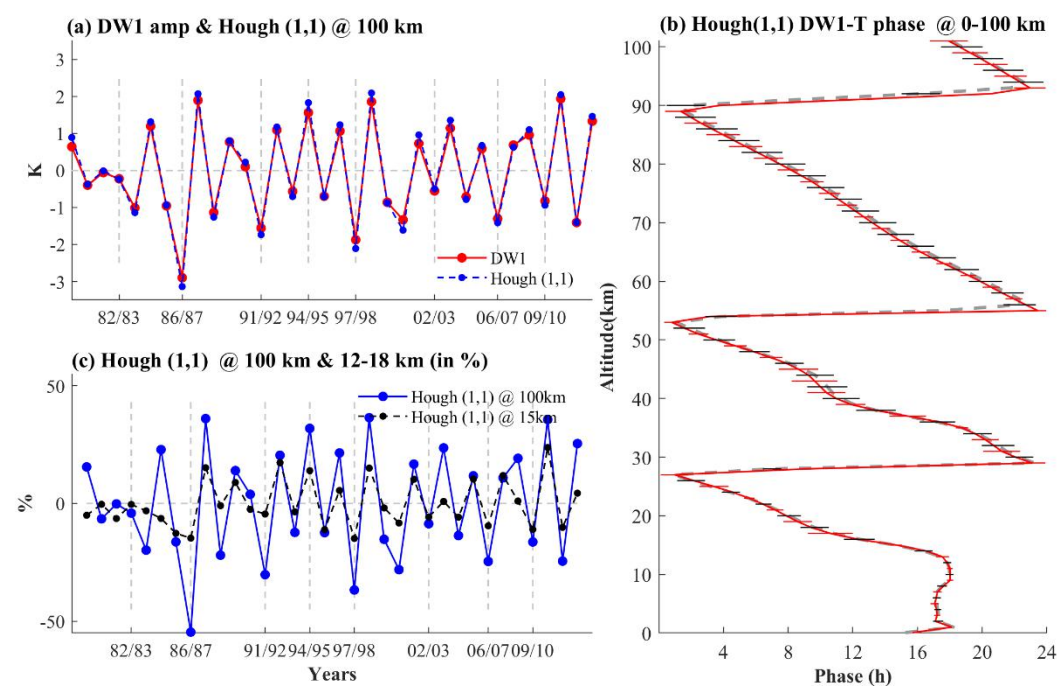
809 confidence levels below 95% for the F test.

810

811

812

删除[author]: 2



814

815 **Figure 4.** (a) The red line indicates the anomalous DW1 temperature amplitude of SD-WACCM
816 simulations averaged over 10°S-10°N at 100 km during the 1979-2013 winter (DJF). The blue line
817 indicates the Hough (1,1) mode of the DW1 temperature amplitude residual at 100 km during the
818 1979-2013 winter (DJF). (b) The thin black line indicates the Hough (1,1) DW1-T phase of
819 SD-WACCM simulations at 0-100 km during the 1979-2013 winter (DJF). The thick black
820 horizontal line indicates the standard deviation of the DW1-T phase. The red line is the same but
821 for El Niño winter. (c) The blue line is the same as in (a), and the black line is the same but for 15
822 km.

823

删除[author]: 3

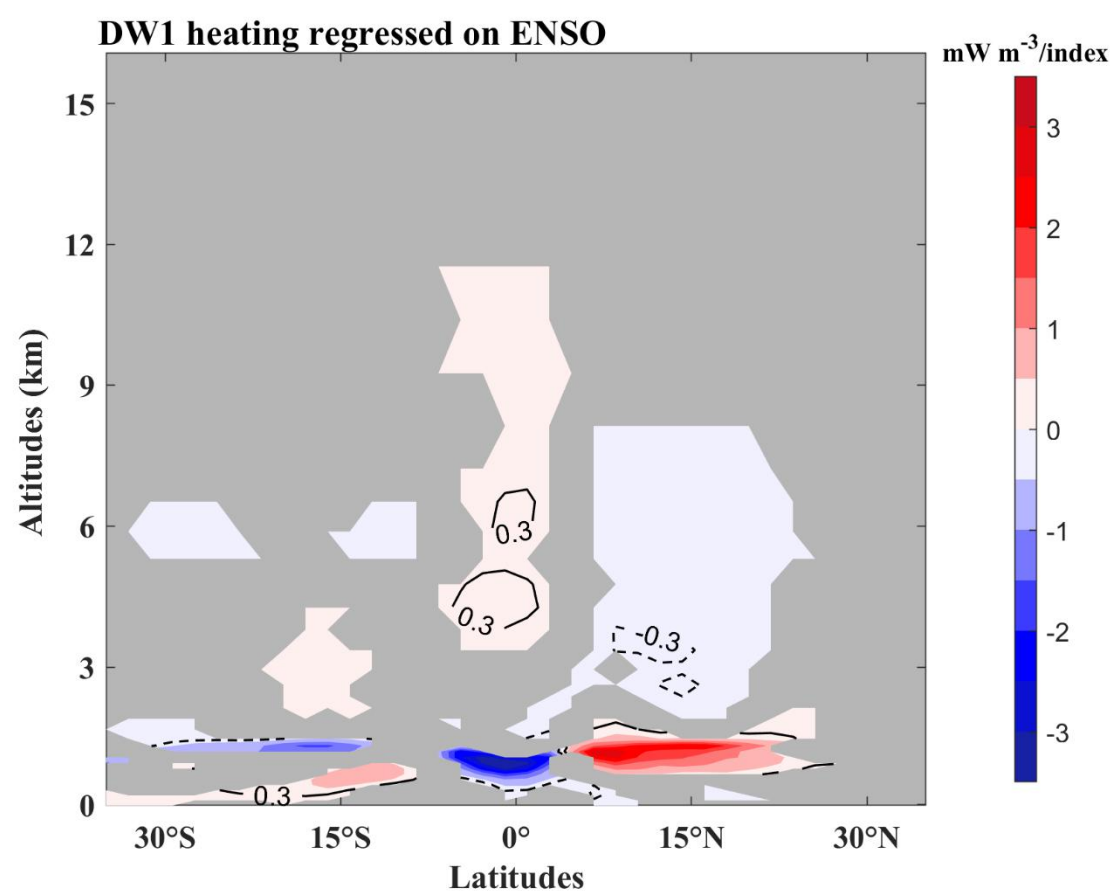


Figure 5. The linear regression coefficient of normalized Niño3.4 in SD-WACCM heating amplitude (mW/m^3 per index) during 1979-2013 winters (DJF). Red represents a positive response, and blue represents a negative response; the grey regions denote confidence levels below 95% according to the F test.

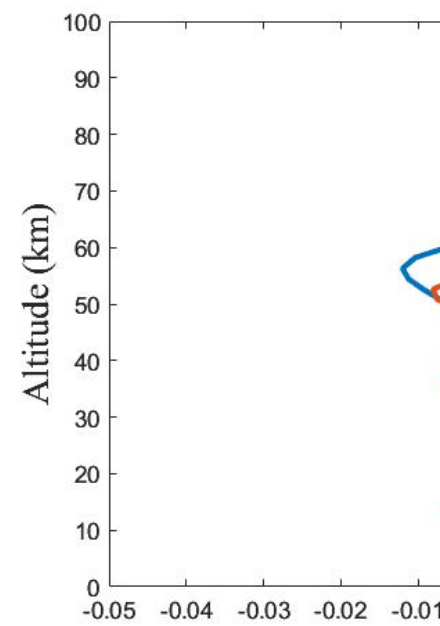
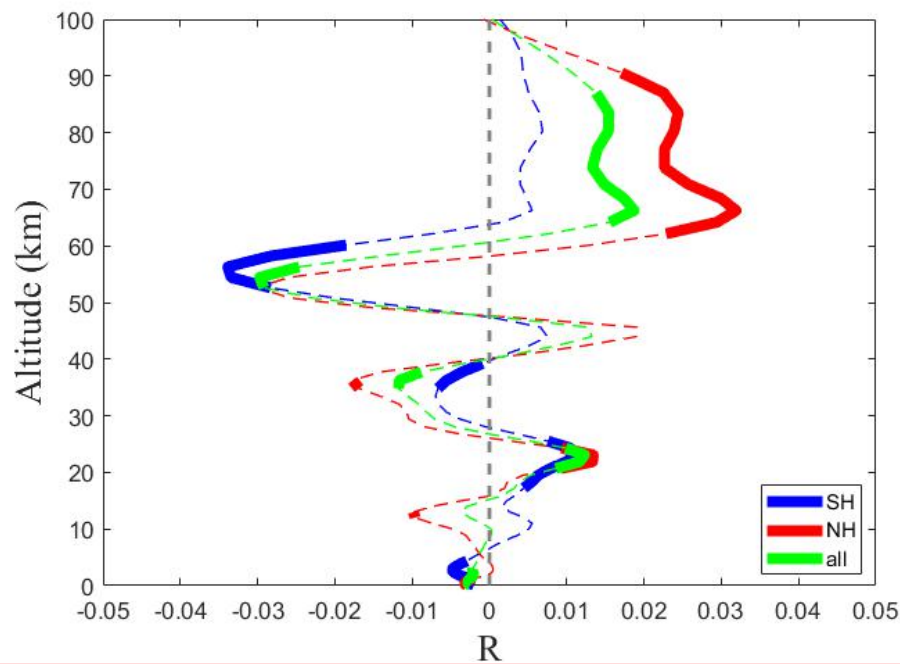


Figure 6. The linear regression coefficient of normalized Niño3.4 in δR (the anomaly of the ratio of the absolute and planetary vorticity). The thin, dashed red, blue and green lines denote the averages of the Northern Hemisphere (from 15°N to 30°N), Southern Hemisphere (from 15°S to 30°S) and the whole (15-30°N and 15-30°S), respectively. The thick, solid lines denote confidence levels below 95% for the F test.

删除[author]:

删除[author]: 5

删除[author]: , δR

删除[author]: thick

删除[author]: solid red and

删除[author]: and

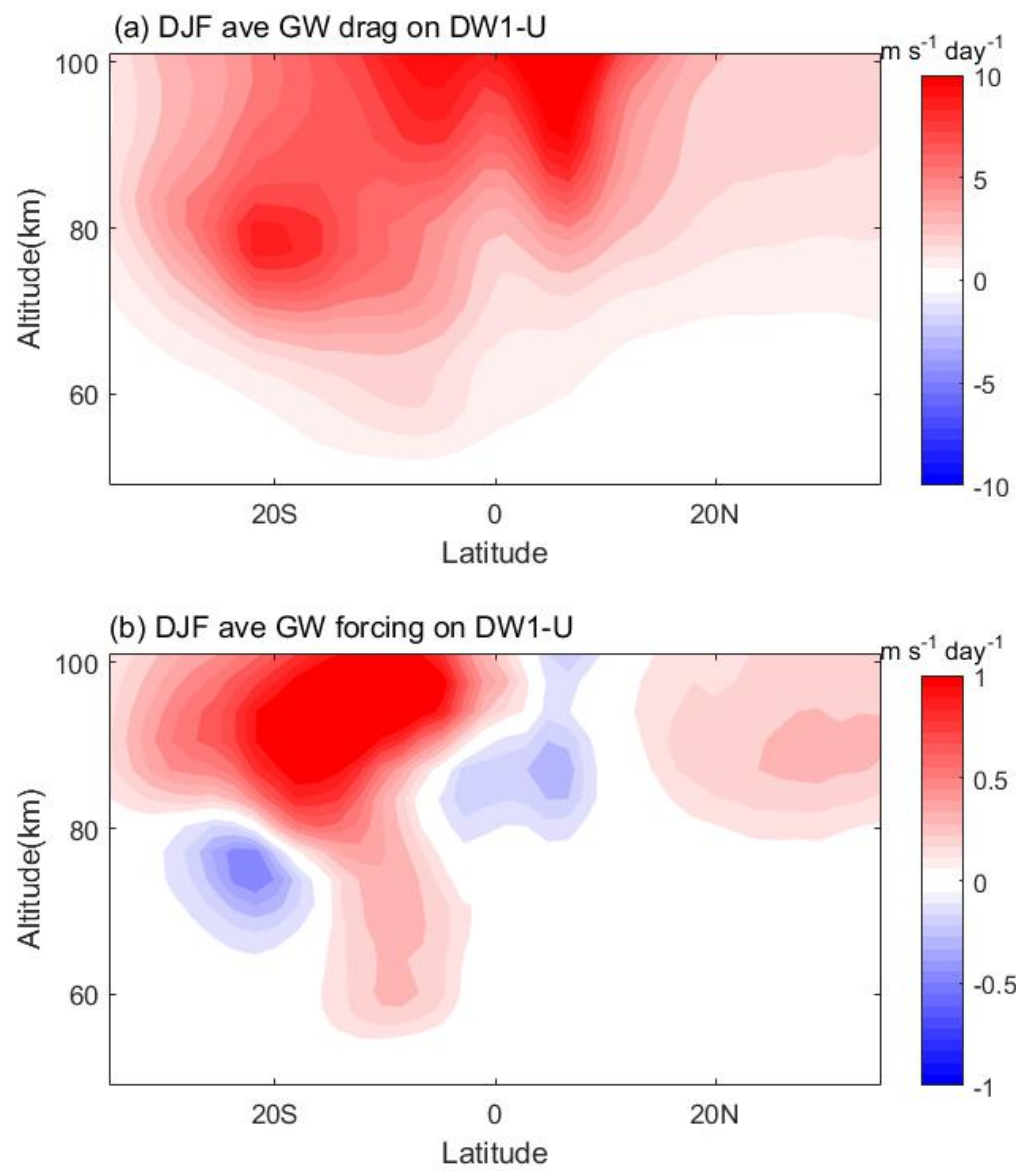


Figure 7. (a) Gravity Wave (GW) drag due to convection on the amplitude of DW1 tidal U during the winter (DJF). (b) The same as (a), but for GW forcing.

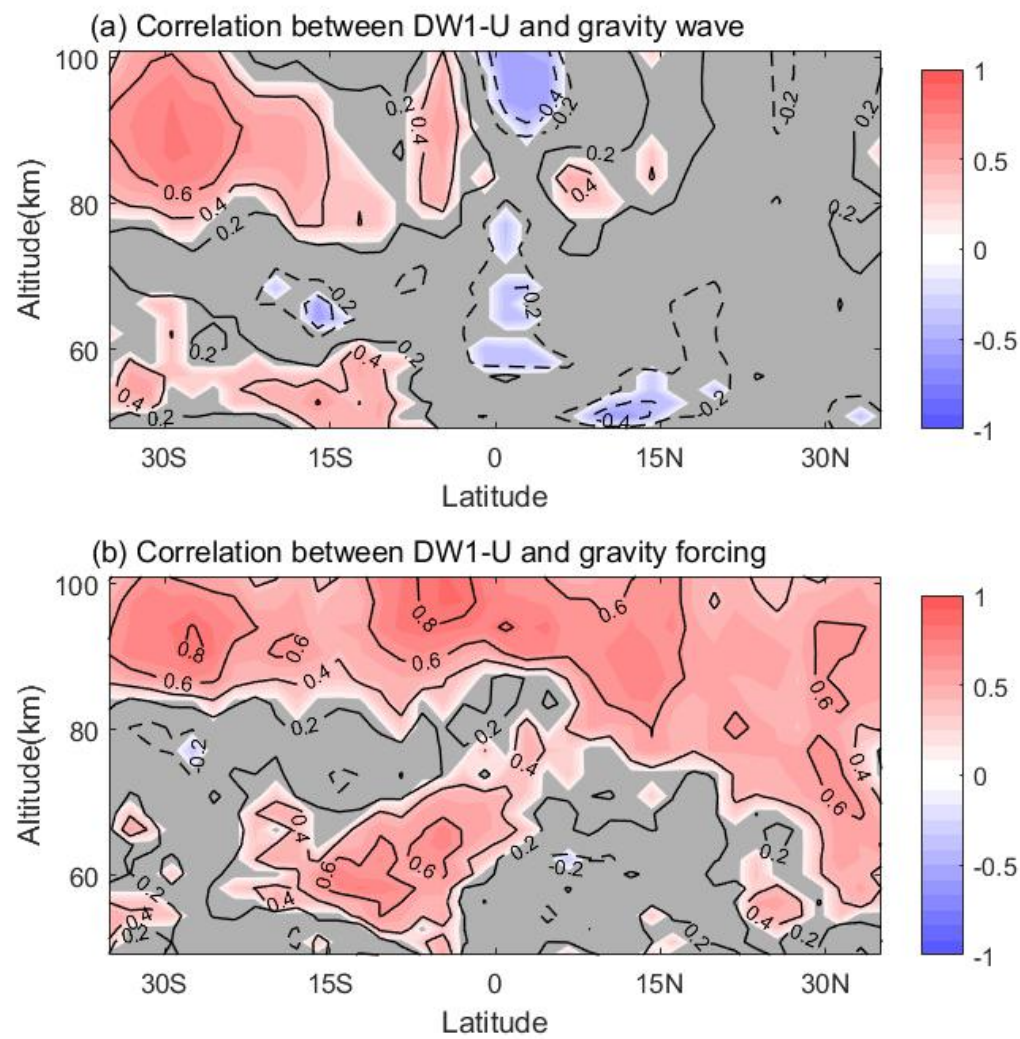


Figure 8. Correlation (a) between DW1 U and GW drag, (b) between DW1 U and GW forcing from 1979 to 2014 winter (DJF).

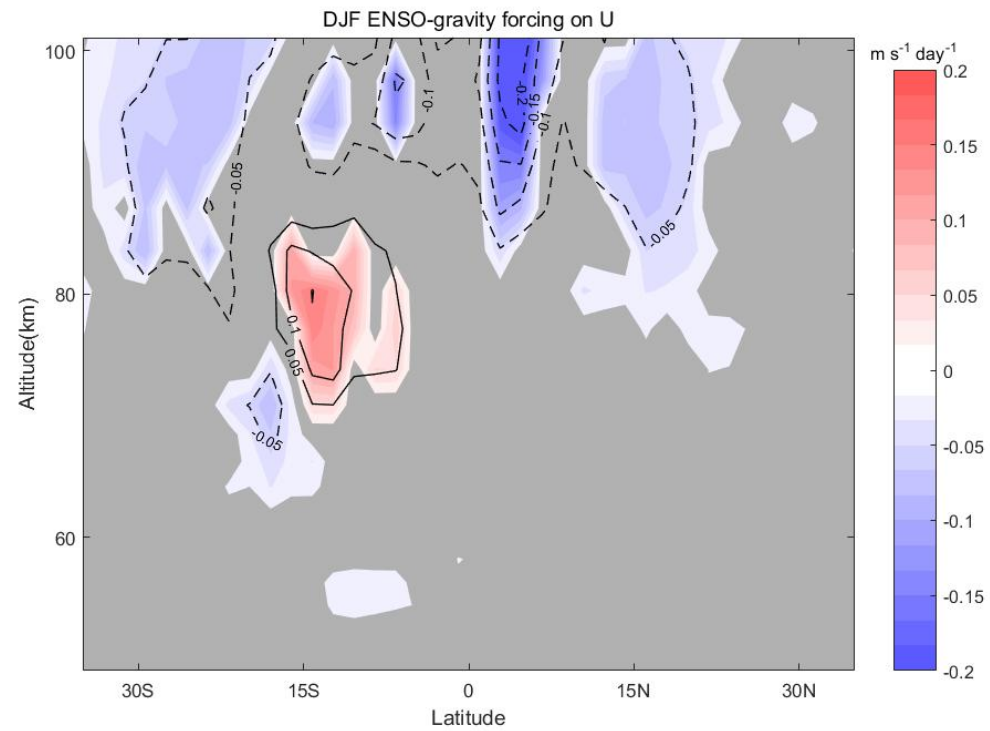


Figure 9. The linear regression coefficient of normalized Niño3.4 in the GW forcing on the amplitude of DW1-U during 1979-2013 winters (DJF). Red represents a positive response, and blue represents a negative response; the grey regions denote confidence levels below 95%.